Research Article

Charge storage properties of mixed ternary transition metal ferrites MZnFe oxides (M = Al, Mg, Cu, Fe, Ni) prepared by hydrothermal method

M. Saghafi[1] · S. A. Hosseini[2] · Sh. Zangeneh[3] · A. H. Moghanian[1] · V. Salarvand[1] · S. Vahedi[1] · Sh. Mohajerzadeh[4]

Abstract

The current investigation focus on synthesize of nano-crystalline mixed ternary transition metal ferrites (MTTMF) through facile hydrothermal method combining post-annealing treatments via tuning the ratio of metallic elements using a nickel foam as the substrate. In this research, different transition metal ferrites of $ZnFe_2O_4$ (ZnFe), CoZnFe oxide, CuZnFe oxide, NiZnFe oxide, AlZnFe oxide and MgZnFe oxide have been synthesized. X-ray diffraction analysis was used to characterize phase development occurred in the MTTMF samples. The Morphologies of the prepared materials have been studied by means of field emission scanning electron microscopy and transmission electron microscopy. The electrochemical performance of the electrodes was evaluated using galvanostatic charge–discharge, AC impedance measurement and cyclic voltammetry analysis. ZnFe electrode prepared at 150 °C shows the highest specific capacitance of 1298 F g^{-1} at 10 mV s^{-1} scan rate in 1 M KOH aqueous solution. It was concluded that higher annealing temperatures (180 °C) for this electrode resulted in better capacitive behavior with specific capacitance of 1580 F g^{-1} at a scan rate of 10 mV s^{-1}. These high performance and great capacitive behavior indicated that the ZnFe electrode is a promising material for energy storage devices.

Keywords Mixed ternary transition metal ferrite (MTTMF) · Supercapacitor · Hydrothermal method · Cyclic voltammetry

1 Introduction

To provide a reasonable amount of energy, demands for energy storage devices with a long cycle life has been raised due to development of new emerging technologies. Besides growing markets for portable electronic devices such as smart watches and phones they need to be flexible, lightweight, compact size, stretchable and more importantly bio-compatible energy storage devices with high power density [1]. Many investigations have been devoted to resolve this issue and also a large number of methods have been proposed by different researchers [1, 2]. In this regard, development of supercapacitors as

energy storage devices have been attracted researcher's attention to fulfill the endlessly rising energy needs in the world and tackling environmental worries due to their high power density and excellent cycle stability. Supercapacitors (SCs) categorize into three classes based on their particular applications: (1) industries and motionless consumers, (2) vehicles and transportation systems, (3) portable and light-weight personal devices. Nanomaterials for electrodes have been broadly examined in SCs as a result of their high surface area, short length of diffusion path and high-power density. In general, the most prominent electrochemical energy storage devices are Lithium-ion (Li-ion) batteries [3], and symmetric and

asymmetric supercapacitors [4]. Supercapacitors are also classified chemically into two different classes; electrical double layer capacitors (EDLC) and pseudo-capacitors. In the former case, energy is stored by electrostatic charges for the carbon materials at the electrode/electrolyte interface with non-faradaic redox reactions while the latter one stores energy by collecting charges electrochemically in the electrode/electrolyte interface with faradaic reversible redox reactions for metal oxides and polymers [5, 6]. Among all the materials as an electrode for SCs or Li-ion batteries purposes, Transition Metal Oxides (TMOs) or Mixed Transition Metal Oxides (MTMOs) such as MFe_2O_4 (M = Ni, Co, Cu and Zn) [7–10], which are known as spinel metal ferrites, and MCo_2O_4 (M = Cu, Ni, Zn, Mg and Mn) [11–15] can upgrade energy density of storage devices. MTMOs possess complex chemical compositions and multiple valences of their metal cations enhanced electrochemical behavior of SCs [16]. Ferrites ability has several redox states and its high permeability is considered as a breakthrough in making appropriate electrodes for SCs [17]. In other words, M and Fe ions in ferrite oxides both play a significant role together to make richer redox reactions than non-ferrite metallic oxides that just has metal ion contribution in the reactions. Therefore, spinel metal ferrites are catalytically active at the surface of electrodes where the ratio of divalent ions is a key factor in order to control surface properties of the electrodes. In addition, the small size and large number of cations in nano-crystallites improve the chemical reactions rate and nowadays are becoming more popular as reactive nano-crystallites [18]. Finally, it should be noted that charges storing in MTMOs originates primarily from the pseudo-capacitive mechanism [19].

Among the metal oxides, properties such as bio-compatibility, high surface to area ratio, great stability and also conductivity of $ZnFe_2O_4$ have made this oxide as an interesting material for SCs [20]. $ZnFe_2O_4$ is fabricated in different shapes and types such as nanowires [12], nanorods [21], nanosheets [22] and nanotubes [23]. Moreover, they play a complicated effective role in battery applications in the shape of $ZnCo_2O_4$ microspheres [24], mesoporous [25] and yolk-shelled particles [26]. So far, different metal oxides or hydroxide nanostructures have been produced to evaluate supercapacitors performance [27, 28]. It is well known that fabrication procedure, active materials mass, measurement methods, and materials microstructure have serious effects on the electrochemical performance of SCs. Therefore, several factors such as chemical composition, sintering time and temperature, preparation conditions as well as dopants determine electrical properties of spinel ferrites [29]. In this regard, wet chemical methods such as microwave-hydrothermal [30–32], co-precipitation reaction [33], solvothermal [34], hydrothermal [35, 36]

and micro-emulsion [37, 38] methods have been used to optimize the production properties. Among them, hydrothermal process [39, 40] has been recognized as the most notable approach to make ferrite powders, while several studies [30, 36, 41–43] proved that holding reaction temperature higher than 130 °C is also necessary. In this study, we describe a facile hydrothermal process to produce MTTMF nanocomposites. Structural and surface morphological characteristics of the synthesized nanocomposites are evaluated and supercapacitive behavior of electrodes has been assessed in 1 M KOH electrolyte through different examination techniques.

2 Experimental

### 2.1 Reagents, materials and synthesis

All the chemical reagents were purchased from Merck and Fluka chemical companies without any further purification. The chemical substances used in this work were nickel nitrate hexahydrate ($Ni(NO_3)_2 \cdot 6H_2O$), copper nitrate trihydrate ($Cu(NO_3)_2 \cdot 3H_2O$), cobalt chloride hexahydrate ($CoCl_2 \cdot 6H_2O$), zinc nitrate hexahydrate ($Zn(NO_3)_2 \cdot 6H_2O$), iron chloride hexahydrate ($FeCl_3 \cdot 6H_2O$), aluminum nitrate nanohydrate ($Al(NO_3)_3 \cdot 9H_2O$), Mg nitrate hexahydrate ($Mg(NO_3)_2 \cdot 6H_2O$), urea ($CO(NH_2)_2$), ammonium fluoride (NH_4F), potassium hydroxide (KOH) and hydrochloric acid (HCl). In addition, a piece of Ni foam was also used as the electrode's substrate.

2.2 Sample characterization

The surface characteristics and structure of the materials were inspected by X-ray Diffraction (XRD) with copper target (Kα, λ = 1.5406 A°) in the range of 10°–70° with 0.04° and 2 θs⁻¹ step size. Raman spectra data were recorded and stored on a Renishaw Raman instrument. The Fourier Transform Infrared (FTIR) spectra of the samples was logged by a spectrometer (FTS 165, wave number from 500 to 4000 cm⁻¹). The morphologies and the sizes of the as-prepared samples were observed using Field Emission Scanning Electron Microscopy (FESEM, Hitachi S4160, 15 kV) and Transmission Electron Microscopy (TEM, PHILIPS, CM30).

2.3 Synthesis of MTTMF thin film

A 100 mL autoclave chamber (with no agitation) was utilized successfully to carry out the hydrothermal synthesis. Ni foam pieces were used in the current investigation as the substrates and before using, they were washed in HCl acid (2 M), Acetone and distilled water, respectively,
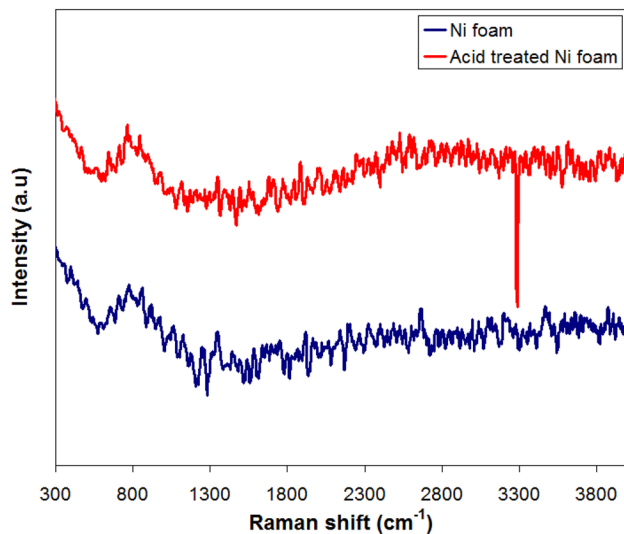
Fig. 1 Raman spectra of Ni foam after and before acid treatment

followed by ultrasonic treatment (35 min for each steps) to remove any oxide layer. The cleaned Ni foam pieces were kept at 60 °C in an oven for 1 h to become dry. RAMAN test was applied before and after acid cleaning of Ni foam while in results related to the after cleaning test s strong peak at 3300 cm^{-1} was detected that could be assigned to OH$^-$ bond (Fig. 1). In fact with this method elemental ions could attach to foam surface easily during hydrothermal method.

To produce the ZnFe$_2$O$_4$ electrode (ZnFe), stoichiometric amounts of Zn and Fe ions (1:2) in the solution were used. It was began by dissolving 3.33 mL of 0.01 M (Zn(NO$_3$)$_2$·6H$_2$O) and 6.66 mL of 0.01 M iron chloride hexahydrate (FeCl$_2$·6H$_2$O) in 100 mL of double distilled water. Then, the mixture was co-precipitated during adding 10 mL of 0.02 M ammonium fluoride (NH$_4$F) and 10 mL of 0.05 M urea to the 100 mL prepared solution. Afterward, a well-cleaned piece of nickel foam was soaked in the solution poured into the autoclave which was sealed for the hydrothermal treatment. The temperature was kept at 150 °C and 180 °C for 5 h, and then the autoclave was cooled down to room temperature. Finally, the products were rinsed with deionized water several times to remove any contaminations or loose bonds and then they were left at 300 °C for an hour to dry. In order to synthesis CoZnFe, CuZnFe, NiZnFe, AlZnFe and MgZnFe oxides, the half of Zn ions in the solution was replaced with Co, Cu, Ni, Al, Mg ions in the solution using a same method to prepare the electrodes active materials. For example, to prepare CoZnFe oxide electrode, the CoCl$_2$.6H$_2$O (1.66 mL of 0.01 M), Zn(NO$_3$)$_2$·6H$_2$O (1.66 mL of 0.01 M), FeCl$_2$·6H$_2$O (6.66 mL of 0.01 M) were mixed with CO(NH$_2$)$_2$ (10 mL of 0.05 M) and NH$_4$F (10 mL of 0.02 M) into 100 mL deionized water.

Table 1 shows the stoichiometric amounts of different ions dissolved in 100 mL of double distilled water to prepare the desired different electrodes.

2.4 Electrochemical characterization

The metal ferrites samples were investigated for supercapacitor applications by an electrochemical cell equipped with a three-electrode measurement system. The galvanostatic charge–discharge, electrochemical impedance analysis and Cyclic Voltammetry (CV) experiments were executed using Autolab PGSTAT 302 N potentiostat. CV curves were obtained at scan rates of 10 to 200 mV s^{-1}. The electrochemical cell was made up of platinum and saturated calomel electrode (SCE), as the counter and reference electrodes, respectively while the prepared thin film on the nickel foam was the working electrode and 1 M KOH was used as the electrolyte. From CV curves, the specific capacitance of the thin films were calculated by the following Eq. 1 [44]:

$$C_{sp}\left(F\,g^{-1}\right) = \frac{\int_{V_a}^{V_b} I \cdot dV}{m \cdot S \cdot \Delta V} \tag{1}$$

where, 'C_{sp}' represents the specific capacitance (F g^{-1}), '$\int I \cdot dV$' is equal to the area enclosed by the CV diagram, 'ΔV' is the applied potential window, 'S' stands for the scan rate (mV s^{-1}) and 'm' designates the deposited mass of the sample material on the nickel foam substrate. The galvanostatic charge–discharge experiments were conducted over a potential window from 0 to 0.5 V at 20 A g^{-1} density

Table 1 The stoichiometric amount of different ions dissolved in 100 mL of double distilled water to prepare different electrodes
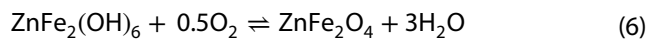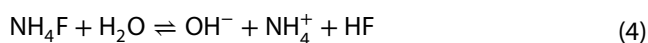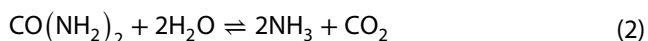
Sample	Ions	Stoichiometry
CoZnFe	Co	0.5
	Zn	0.5
	Fe	2
AlZnFe	Al	0.5
	Zn	0.5
	Fe	2
MgZnFe	Mg	0.5
	Zn	0.5
	Fe	2
CuZnFe	Cu	0.5
	Zn	0.5
	Fe	2
NiZnFe	Ni	0.5
	Zn	0.5
	Fe	2
ZnFe	Zn	1
	Fe	2

current. The electrochemical impedance spectra (EIS) was taken over the frequency range of 10–100 kHz.

3 Results and discussion

The schematic depicted in Fig. 2 illustrates the preparation method of ZnFe on the nickel foam substrate. The film produced by a heterogeneous reaction and its growth kinetics follows the ion-by-ion growth principle. The zinc and iron hydroxides participate in this regard and are absorbed by the nickel foam nucleation sites. The process consists of three steps: first, the nucleation or incubation time followed by the growth period. In this step, several chemical reactions take place in the deposition bath based on the participated materials, then in the growth period the film thickness increases linearly proportional to the deposition time. At this time, the solution concentrate from ionic product above its solubility and therefore the solution become supersaturated maximally leading to the nuclei growth and the film deposition. As the reagent becomes depleted in the solution, the film thickness growth stops and the process will be terminated. Ni foam electrodes with mesoporous ZnFe or other metal ferrite thin films make a strong contact between the substrate and the active material, which contributes to transportation of electrons and ions and therefore forms a low contact resistance with great electrochemical properties.

The hydrothermal method followed by calcination at 300 °C was used to synthesize the ZnFe electrode by the following reactions. At the first, $CO(NH_2)_2$ and NH_4F dissociate in water during heating at a high temperature (150 and 180 °C). Afterwards, zinc and iron ions (1:2 molar ratio) react with OH^{-1} and uniformly precipitate on the surface of the Ni foam under the hydrothermal condition. In the next step, Zn-Fe hydroxide transform into Zn-Fe oxide by calcination at 300 °C. The reactions are summarized as follow:

$$CO(NH_2)_2 + 2H_2O \rightleftharpoons 2NH_3 + CO_2 \tag{2}$$

$$NH_3 + H_2O \rightleftharpoons OH^- + NH_4^+ \tag{3}$$

$$NH_4F + H_2O \rightleftharpoons OH^- + NH_4^+ + HF \tag{4}$$

$$2Fe^{+2} + Zn^{+2} + 6OH^- \rightleftharpoons ZnFe_2(OH)_6 \tag{5}$$

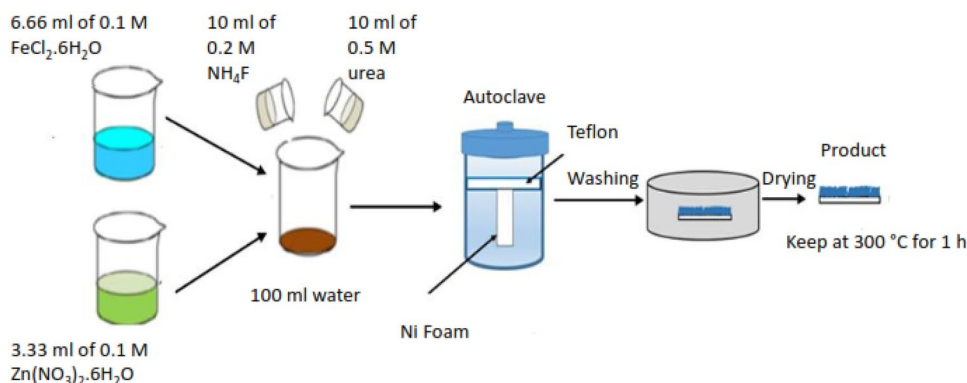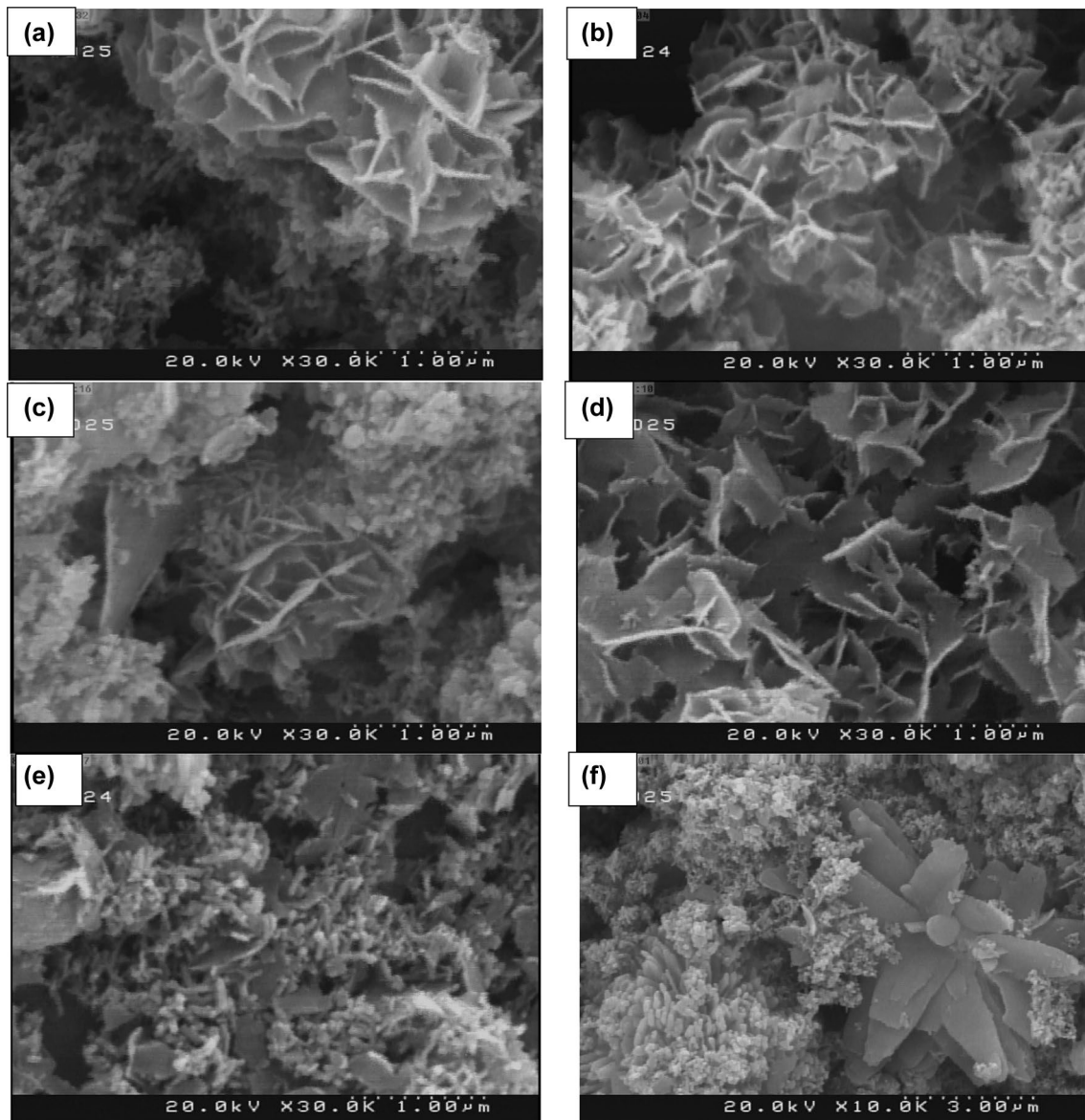$$ZnFe_2(OH)_6 + 0.5O_2 \rightleftharpoons ZnFe_2O_4 + 3H_2O \tag{6}$$

In order to clarify the mechanism of metallic ferrite nanocrystalline development over the nickel foam, the grown products at two different temperatures (150 and 180 °C) in the post-annealing treatment were investigated by FESEM. The MTTMF precursors coated on the substrate present intriguing structures with three different morphologies (depending on the reaction temperature 150 °C and 180 °C) were observed: nano wires, flower-like nano flakes and nano particles. In Fig. 3a–f numerous flower-like nano flakes and nano wires is shown covered the skeleton of Ni foam.

By changing the hydrothermal temperature from 150 to 180 °C, the nanostructures transformed from nano flakes to inter connected porous nano particles, as shown in Fig. 4b, c, e, f, in which annealing of materials led to formation finer crystalline morphologies. Also, it was revealed that as the temperature increased, the thin films became more porous. The pores formation could be ascribed to the release of CO_2 and H_2O during the heating treatment of the precursor which increases the surface area. It seems that, nano-porous thin films formation for supercapacitors result in an excellent electrochemical performance of the devices because of their high surface to area feature, easy ions transportation and extra active sites for the fast reversible faradaic redox reactions.

Figure 5a–f show TEM images of MTTMF nanostructures which are composed of many flakes, wires and sheets with different sizes. However, for the ZnFe prepared at 180 °C (Fig. 5d) a unique microstructure was detected which contained a large surface to area in order to improve electrochemical performance. As it is visible in Fig. 5e–f some well-defined nano particles with thin hexagonal platelets were observed by SEM observations. In the nucleation stage during the hydrothermal process, numerous

**Fig. 2** Schematic presentation of preparation method of ZnFe electrode

6.66 ml of 0.1 M FeCl$_2$.6H$_2$O

10 ml of 0.2 M NH$_4$F

10 ml of 0.5 M urea

Autoclave

Teflon

Washing

Drying

Product

Keep at 300 °C for 1 h

100 ml water

Ni Foam

3.33 ml of 0.1 M Zn(NO$_3$)$_2$.6H$_2$O

Fig. 3 FESEM images of **a** ZnFe, **b** CoZnFe, **c** MgZnFe, **d** NiZnFe, **e** CuZnFe, **f** AlZnFe prepared at 150 °C for 5 h

$ZnFe_2O_4$ precursor nano-seeds derived from combination of the Zn^{2+}, Co^{+2} and OH^{-1} ions. With the reaction proceeding, the crystal growth stage transferred to a kinetically controlled process, and small nano-wires or nano-sheets began to grow from the nucleation site depending on growths mechanism. As the autoclave temperature increased from the 150 to 180 °C, kinetics of the reaction were changed in terms of the nucleation, aggregation, coalescence and growth rate of CuZnFe and AlZnFe samples. The increasing temperature altered Brownian motion or short-range interaction of the solution particle. What is more, it changed inside pressure of the autoclave, modifying the surface morphology from nanowires to nanoparticles. The increasing temperature limits vertical growth of

the nanomaterial, which reduces its surface energy. The hydrothermal method works on principle of controlled precipitation under influences of temperature, pressure and composition of dissolved ions in the hydrothermal autoclave reactor. The increasing reaction temperature may alter chemical reaction rate, which leads to formation of different nanostructures.

FTIR spectra of different samples are presented in Fig. 6. Usually, ions in the crystal lattice have specific peaks associated with their vibrations could be detected in the range of 500 to 4000 cm^{-1} [45]. Consequently, the band in the frequency range of 555–600 cm^{-1} could be assigned to the tetrahedral complexes of spinel ferrites [46]. The vibration bands at 1625 cm^{-1} and 3460 cm^{-1} could be associated to
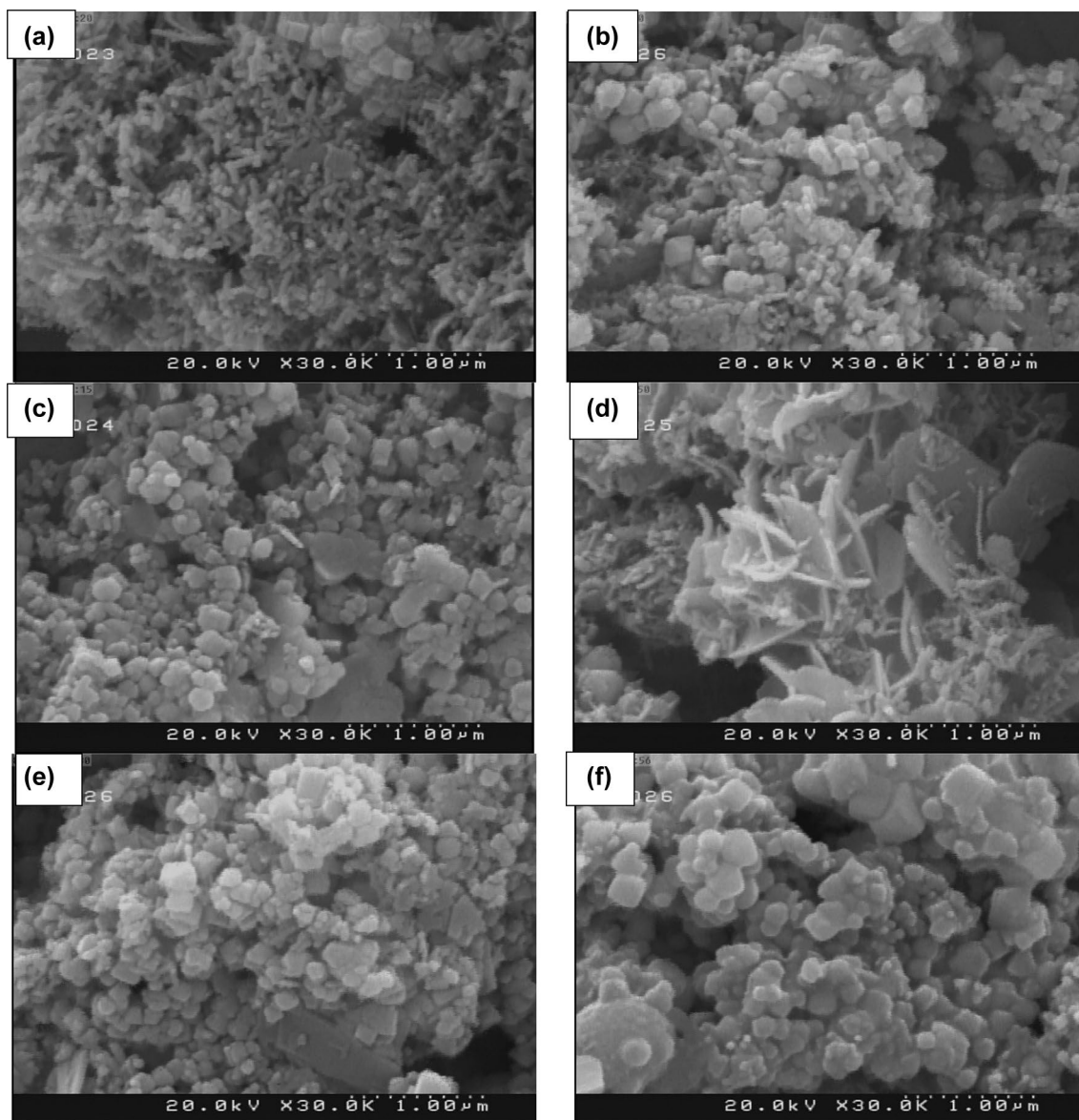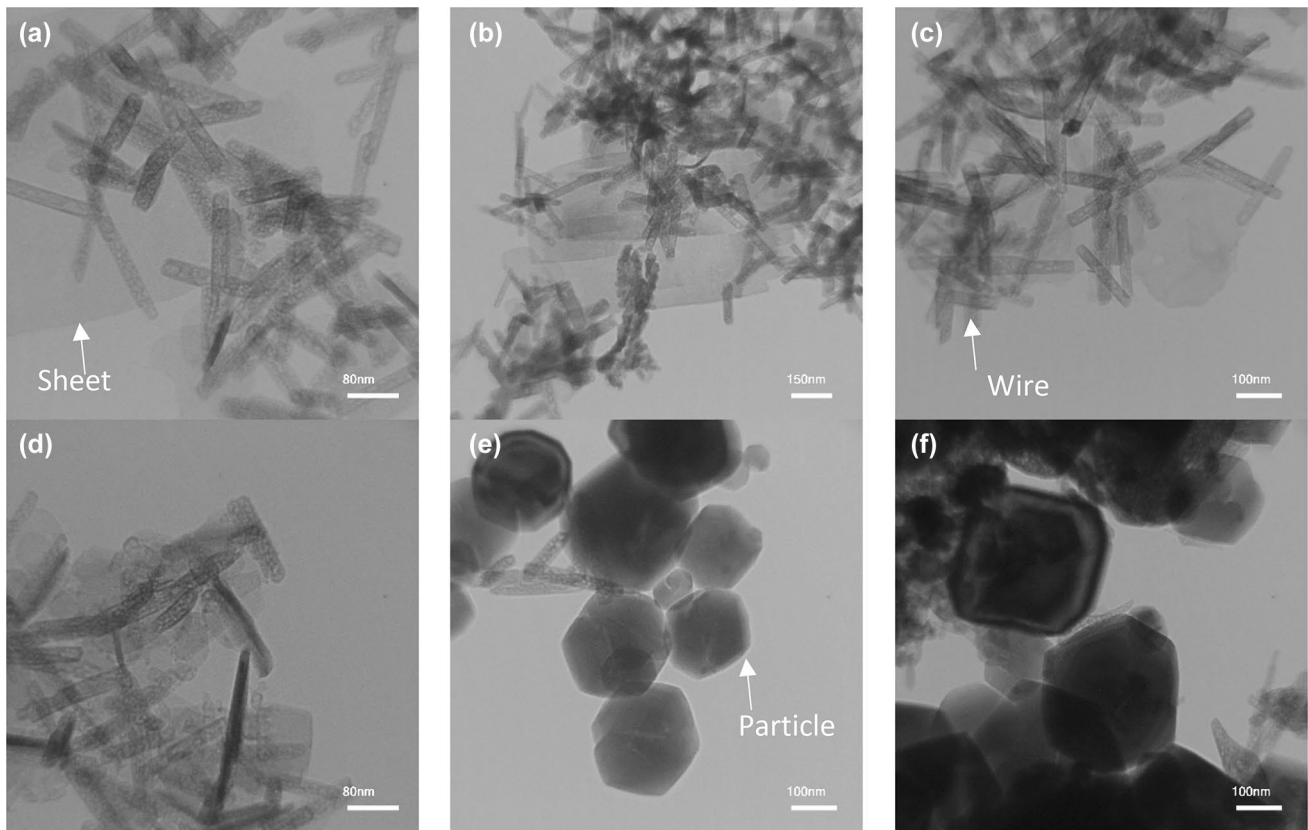
Fig. 4 FESEM images of **a** ZnFe, **b** CoZnFe, **c** MgZnFe, **d** NiZnFe, **e** CuZnFe, **f** AlZnFe prepared at 180 °C for 5 h

O–H bending and stretching, respectively, this is related to water absorption on the ferrite nanomaterial surfaces [47]. In other samples at 3460 cm^{-1}, there is a peak corresponding to O–H stretching, however, in CoZnFe, the O–H peak was slightly moved to higher frequencies with a lower magnitude as a result of hydroxides release to form oxides [16]. In addition, the peak at 1125 cm^{-1} is connected to Zn–O–Fe bond formation. Moreover, in ZnFe hydroxide, a peak was observed at 1095 cm^{-1} reveals the presence of iron oxide hydroxide bonds (γ-FeOOH) [13].

X-ray diffraction (XRD) patterns of the different samples (ZnFe, CuZnFe, CoZnFe, AlZnFe, MgZnFe, NiZnFe) synthesized via the hydrothermal method are shown in Fig. 7. To avoid the results interferences, MTTMF films were

separated from the nickel substrate. All the samples exhibit the features of ferrite materials with the strongest peak at (311) occurred at around 2θ = 36° and therefore verify their cubic spinel structure. XRD results were the same as the $ZnFe_2O_4$ JCPDF card: 89-4926 standard spectra. In the XRD results of the ZnFe electrode, the strong peaks at 32.5°, 41°, 55.2°, 56.9°, 62.5° could be indexed to (220), (311), (400), (422), (511), (400) planes of $ZnFe_2O_4$ phase. XRD patterns indicate that CuO (tenorite, JCPDS card No. 48–1548), cubic Cu_2O (cuprite, JCPDS card No. 05-0667) exist in the CuZnFe sample. The peaks of the prepared CoZnFe sample can be attributed to CoO (JCPDS card No. 48-1719) [48]. XRD results of all these MTTMF materials

Fig. 5 TEM images of **a** ZnFe, **b** CuZnFe, **c** AlZnFe prepared at 150 °C for 5 h, **d** ZnFe, **e** CuZnFe, **f** AlZnFe prepared at 180 °C for 5 h
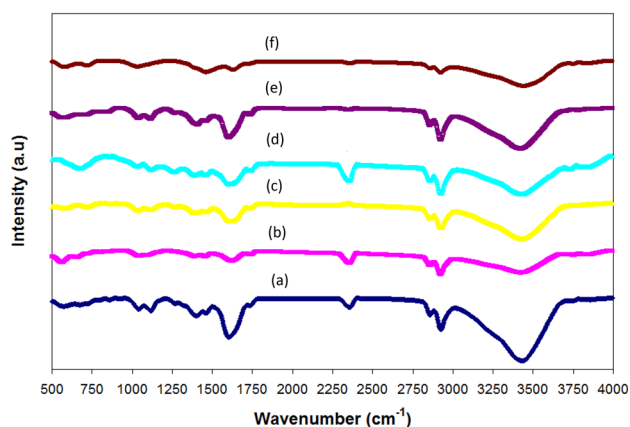
Fig. 6 FTIR spectra of **a** ZnFe, **b** CoZnFe, **c** MgZnFe, **d** NiZnFe, **e** CuZnFe, **f** AlZnFe electrodes prepared at 150 °C for 5 h
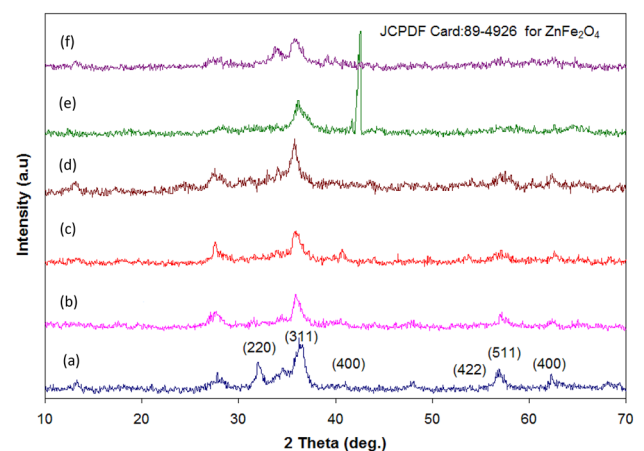

Fig. 7 XRD of **a** ZnFe, **b** AlZnFe, **c** MgZnFe, **d** CuZnFe, **e** CoZnFe, **f** NiZnFe electrodes prepared at 150 °C for 5 h

disclose significant wide peaks, which could be related to the presence of infinitesimal crystallites [49].

A three electrodes cell system was used to investigate the supercapacitive properties of the electrodes produced in different heat treatment temperatures. CV of MTTMF thin films was examined at different scan rates (rate capability). In this regard, Figs. 8 and 9 show

CV curves obtained from all the MTTMF thin films prepared at 150 and 180 °C in 1 M KOH electrolyte at different scan rates of 10–200 mV s^{-1} in the voltage range of -0.5 to 0.5 V, respectively. In the higher scan rates, the area under the curves is larger which results in higher redox peaks at the maximum current density along with
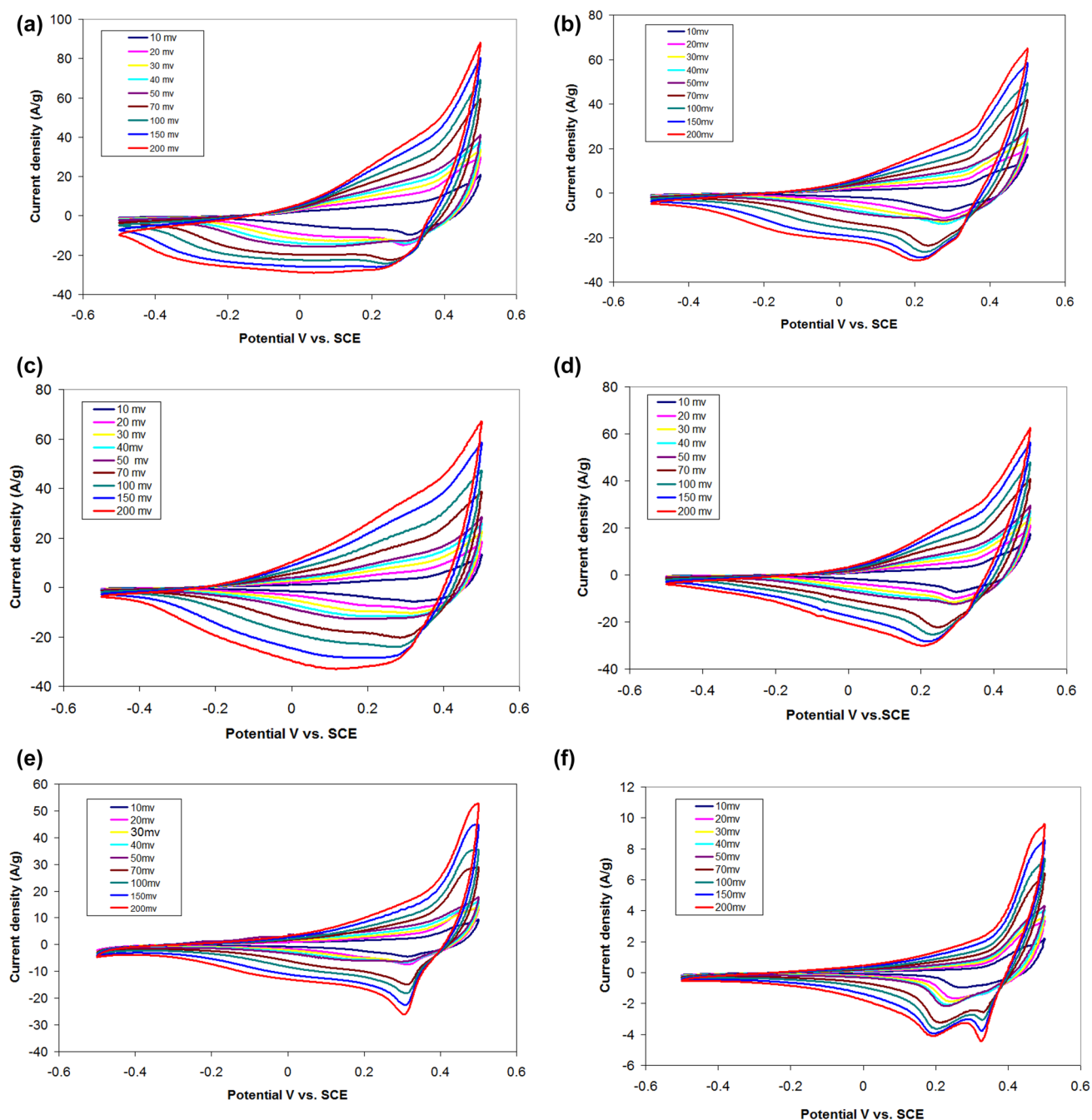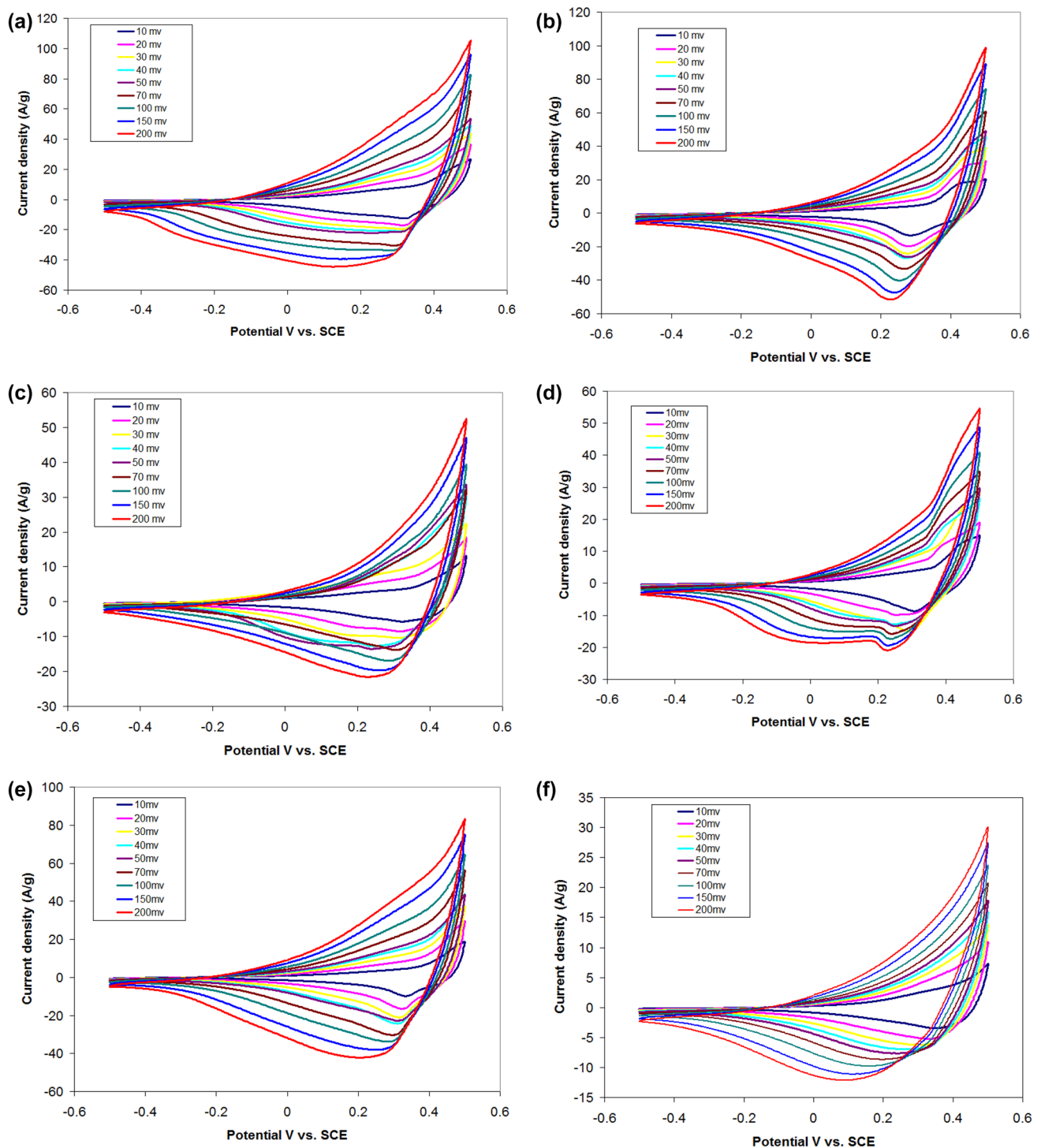
Fig. 8 CVs of **a** ZnFe, **b** CoZnFe, **c** MgZnFe, **d** NiZnFe, **e** CuZnFe, **f** AlZnFe electrodes at different scan rates of 10 up to 200 mV s^{-1} prepared at 150 °C 5 h

a lower specific capacitance. There are various redox peaks for each sample due to the faradaic redox reactions between metal oxide and metal oxide hydroxide bonds in each MTTMF samples [50].

All the MTTMF thin film electrodes responses at 150 °C are presented in Fig. 8 and a similar sequence of images for the samples prepared at 180 °C is depicted in Fig. 10. Unfortunately, the voltammogram did not define well

the presence of the oxidation/reduction peaks. They are unlike the EDLCs where the CV has ideally a rectangular form signifying their pseudocapacitive behavior [51]. For instance, in Fig. 8a a pair of redox peaks would bring to mind that the capacitance is caused from a pseudocapacitive property like reversible electrochemical reactions associated to Zn (or Fe)-O/Zn(or Fe)-O-OH although they are typical faradaic behavior of ZnFe in

Fig. 9 CVs of **a** ZnFe, **b** CoZnFe, **c** MgZnFe, **d** NiZnFe, **e** CuZnFe, **f** AlZnFe electrodes at different scan rates of 10 up to 200 mV s^{-1} prepared at 180 °C 5 h

such electrolytes. Also, there are principal differences between pseudocapacitive, EDLC, battery and other storage devices in their shape of CVs. In general, pseudocapacitive behavior doesn't only depend on the linear relation between the stored charge to the potential window (or the scan rate) [52], therefore, we must denote these MTTMF electrode materials as typical energy storage devices to make it clear for further researches.
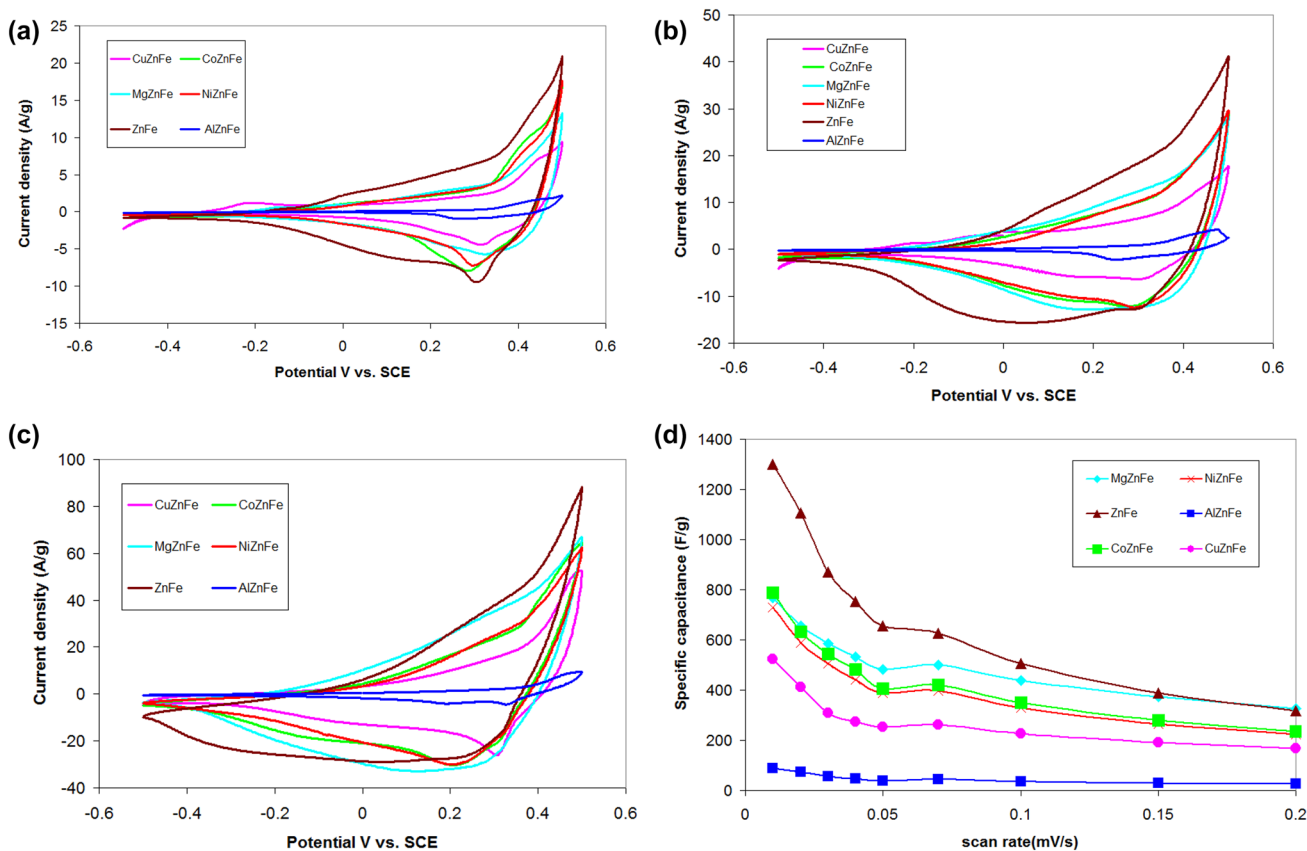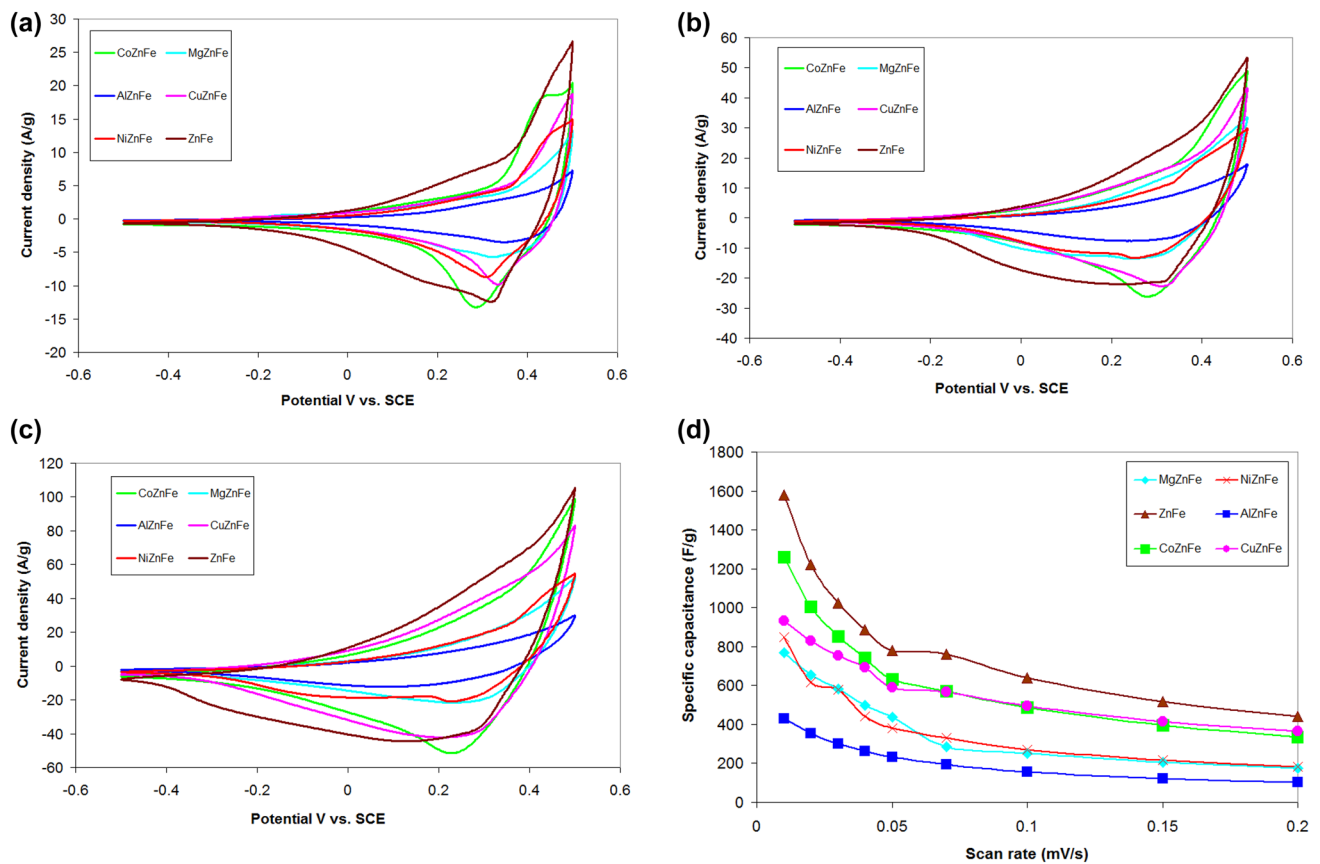
Fig. 10 CVs of all electrode at **a** 10 mV s^{-1} **b** 50 mV s^{-1} and **c** 200 mV s^{-1} prepared at 150 °C 5 h. **d** Capacity dependence of electrodes as a function of scan rate from 10 to 200 mV s^{-1}

Specific capacitance was analyzed by CV results for all the MTTMFs at different scan rates and are shown in Figs. 10 and 11. The results demonstrate the specific capacitance retentions of MTTMFs electrodes as a function of the applied scan rate. The specific capacitance was decreased in higher scan rates as a result of inaccessible sites of pores while in lower charge-discharging rates, ions find enough time to access and utilize outer and inner sites of pores hence the calculated specific capacitance under slow scan rates is considered as the full capacity of the device [53]. The largest specific capacity was about 1298 F g^{-1} at 10 mV s^{-1} scan rate in 1 M KOH aqueous solution for ZnFe electrodes prepared at 150 °C. This figure also shows decreasing of the specific capacity of this electrode with increasing the scan rate to 200 mV s^{-1}. It has been deduced that higher annealing temperatures result in better capacitive behavior based on the CV assessment in which at a scan rate of 10 mV s^{-1} a superior specific capacitance of 1580 F g^{-1} was obtained for the same electrodes prepared under the 180 °C condition. Figures 10d and 11d show the charge storing behavior of the ZnFe electrode decreased with incorporation of another metal oxide to the spinel structure. As shown in these figures, the

specific capacitance of CoZnFe, CuZnFe, NiZnFe, AlZnFe and MgZnFe electrodes is less than ZnFe in all the scan rates. Furthermore, as is shown in Fig. 10d, compared with Fig. 11d, the electrochemical performance was considerably boosted in nearly all of the mixed ternary metal oxides prepared at 180 °C, while, increasing the temperature had no effects on NiZnFe electrode and even had destructive outcomes on MgZnFe electrode.

Metal oxide or hydroxide composites are compared electrochemically in Table 2. Lin et al. [40] reported a porous structure of ZnFe$_2$O$_4$ fabricated by polystyrene (PS) microspheres as a hard-template. The resulted porosity exhibited specific capacitance of 301.8 F g^{-1} at the scan rate of 2 mV s^{-1} and noticeable cyclic stability of 140.97% after 5000 cycles in 2 A g^{-1} current density. The sol–gel method and subsequent calcination resulted in quasi-honeycomb-like biological structures of ZnFe$_2$O$_4$ in which electrode surface area significantly increased and showed high specific capacitance of 279.4 F g^{-1} at 10 mV s^{-1} and 80% capacity retention after 1000 charge/discharge cycles [54]. Lin et al. [55] represented another method to develop promising electrodes in supercapacitors with proper chemical properties. Etched coral-like ZnFe particles with 200

Fig. 11 CVs of all electrode at **a** 10 mV s^{-1} **b** 50 mV s^{-1} and **c** 200 mV s^{-1} prepared at 180 °C 5 h. **d** Capacity dependence of electrodes as a function of scan rate from 10 to 200 mV s^{-1}

**Table 2** Comparing of electrochemical properties of some similar devices with different preparation methods

Material	Electrolyte	Specific capacitance (F g^{-1})	Potential window (V)	Discharge current	Capacity retention	Method	Refs.
Porous ZnFe$_2$O$_4$	6 M KOH	301.8	0.45	2 A g^{-1}	140.97%(5000 cycle)	Template-assisted(polystyrene)	[26]
ZnFe$_2$O$_4$ replica	2 M KOH	279.4	0.55	1 A g^{-1}	80%(1000 cycle)	Sol–gel	[54]
Coral-like ZnFe$_2$O$_4$	3 M KOH	471	− 0.8	1 A g^{-1}	80.6%(3000 cycle)	Etch process	[55]
ZnFe$_2$O$_4$ thin film	1 M NaOH	471	− 0.1	2.72 A g^{-1}	72%(1000 cycle)	SILAR	[56]
ZnFe$_2$O$_4$ nano flake	6 M KOH	2083	0.4	5 mA cm^{-2}	98%(12000 cycle)	Reflux condensation mediated deposition	[57]
ZnFe$_2$O$_4$	6 M KOH	615	–	3 mA cm^{-2}	74% 3000 cycles	SILAR	[58]
ZnFe$_2$O$_4$ nano particle	2 M KOH	352.9	1.2	1 A g^{-1}	92.3% 10000 cycles	Solvothermal	[59]
ZnFe$_2$O$_4$ fibers	3 M KOH	590	0.7	1 A g^{-1}	95% 3000 cycles	Electrospun	[60]
ZnFe$_2$O$_4$ microspheres	1 M KOH	131	0.45	0.1 A g^{-1}	92% 1000 cycles	Solvothermal	[29]
ZnFe$_2$O$_4$	1 M KOH	1580	0.5	10 mV s^{-1}	94% 5000 cycles	Hydrothermal	This work

times larger specific area obtained higher specific capacitance of 471 F g^{-1}. They also displayed excellent cyclic stability of 80.6% specific capacitance retention after 3000 cycles. ZnFe thin films synthesized through a facile and low-priced successive ionic layer adsorption and reaction (SILAR) method, offered 471 F g^{-1} specific capacitance at 5 mV s^{-1} scan rate in 1 M NaOH aqueous solution. ZnFe$_2$O$_4$ solid-state symmetric (SSS) materials also showed great

properties (32 F g^{-1} specific capacitance, 4.47 W h kg^{-1} energy density and 277 W kg^{-1} power density at 1 A g^{-1} current density) reported by Raut et al. [56]. Vadiyar et al. reported utilization of cobalt oxide (Co_3O_4) nanosheets as an active material for the positive electrode and zinc ferrite ($ZnFe_2O_4$) nano-flakes for the negative electrode, which grew directly on a stainless steel (SS) substrate; increased stability up to 12000 cycles with 98% retention of capacitance in solid-state asymmetric assembled devices. This device also stored 36 W h kg^{-1} energy density while the power density was about 8.8 kW kg^{-1} [57]. Vadiyar et al. [58] established the SILAR technique to synthesize nano sphere particles of $ZnFe_2O_4$ with a diameter in the range of 200 to 600 nm on SS substrates. The annealed $ZnFe_2O_4$ thin films demonstrated excellent specific capacitance of 615 F g^{-1} at 3 mA cm^{-2} current density. An asymmetric device was made using two electrodes ($ZnFe_2O_4$/SS||Mn_3O_4/SS) which provided specific capacitance of 81 F g^{-1} and the energy density of 28 W h kg^{-1} while power density was 7.97 kW kg^{-1}. 74% capacitance retention was recorded in 3000 cycles for this device as well. Yang et al. [59] reported at a current density of 1 A g^{-1} specific capacitance of 352.9 F g^{-1}, which showed a superior value as good as other ZnFe based electrodes. It also shows significant cyclic stability (92.3% retention after 10,000 cycles) and good rate performance. Although a low voltage of 1.2 V was applied, the energy density of the ZnFe/rGO (reduced graphene oxide) supercapacitor in a 1 M KOH electrolyte could rise to above 6.7 W h kg^{-1}. Agyemang and Kim synthesized ZnFe-based nanofibers by electro-spinning using ferric/zinc acetonate as the metal oxide precursors and the polyvinyl pyrrolidone (PVP) as the main polymer in different composition ratios. Various produced compositions had distinctive properties for supercapacitor applications. The maximum specific capacitance calculated from the obtained CV curves for the Fe_2O_3–$ZnFe_2O_4$ electrode was 590 F g^{-1} at 5 mV s^{-1} scan rate [60]. Zhu et al. [29] reported feasible and cost effective synthesize of ZnFe microspheres using a solvothermal approach without any template. Characterization of the produced samples revealed that many ZnFe nanoparticles with the size of smaller than 20 nm were assembled to form ZnFe microspheres with a high specific surface in addition to great optical and magnetic properties. Besides these, ZnFe microspheres exhibited excellent electrochemical characteristics with a great cycling life of 92% capacitance retention after 1000 cycles and specific capacitance of 131 F g^{-1}.

Figure 12 illustrates galvanostatic charge–discharge measurements of MTTMF electrodes at 20 A g^{-1} current density under applied potential of voltage between 0 and 0.5 V. Notably, the almost-linear variation of the charge–discharge curves for MTTMF electrodes in addition to their symmetrical triangular shape indicate a suitable
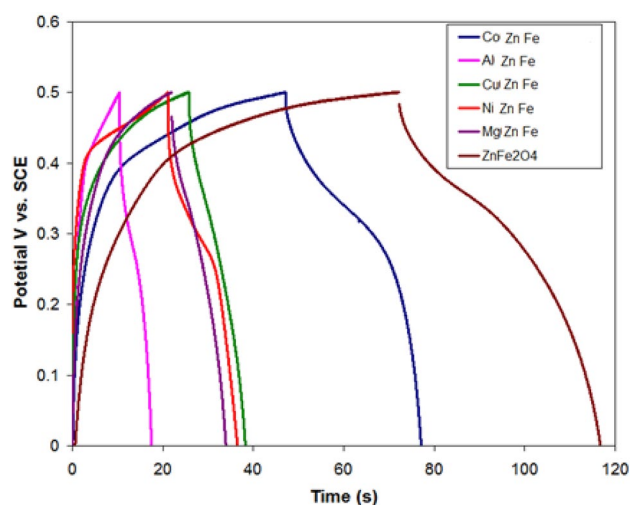
Fig. 12 Galvanostatic charge–discharge curves of electrodes prepared at 180 °C over a potential window between 0 and 0.5 V at 20 A g^{-1} charge–discharge current

capacitive behavior as well as great reversibility [61, 62]. However, for these MTTMF electrodes, redox reaction or irreversible adsorption of electrolyte ions are responsible for the charged potential value. No significant $I \times R$ drop is detected in the curves suggesting a favorable contact between the electrodes and the active material. This figure shows that longer times to charge and discharge ZnFe electrodes was needed rather than other electrodes, which means larger specific capacity for this electrode. The following equations evaluate electrodes maximum specific energy and power:

$$E_{Sp} = \frac{0.5C_{sp}V^2}{3.6}(\text{Wh kg}^{-1}) \tag{7}$$

$$P_{Sp} = \frac{E_{sp}}{\Delta t}(W\ kg^{-1}) \tag{8}$$

where C_{sp} is the specific capacitance, V is the potential after IR drop and Δt stands for the discharge time. Maximum specific energy of ZnFe, CoZnFe, CuZnFe, NiZnFe, AlZnFe and MgZnFe electrodes were measured to be 55.5, 36.11, 13.8, 15.2, 8.3, and 12.5 W h kg^{-1}, respectively at 20 A g^{-1} discharge current. The maximum specific power of electrodes was measured to be 4.99 kW kg^{-1} at 20 A g^{-1} discharge current.

Electrochemical impedance spectroscopy (EIS) is used to estimate supercapacitor properties of the electrodes by relating their structure to the molecular relaxation of the system measured in a wide range of frequencies [63]. In MTTMF electrodes, electrochemical impedance was measured in the frequencies of 0.1 Hz–10 kHz with an applied potential magnitude of 5 mV. The EIS data were
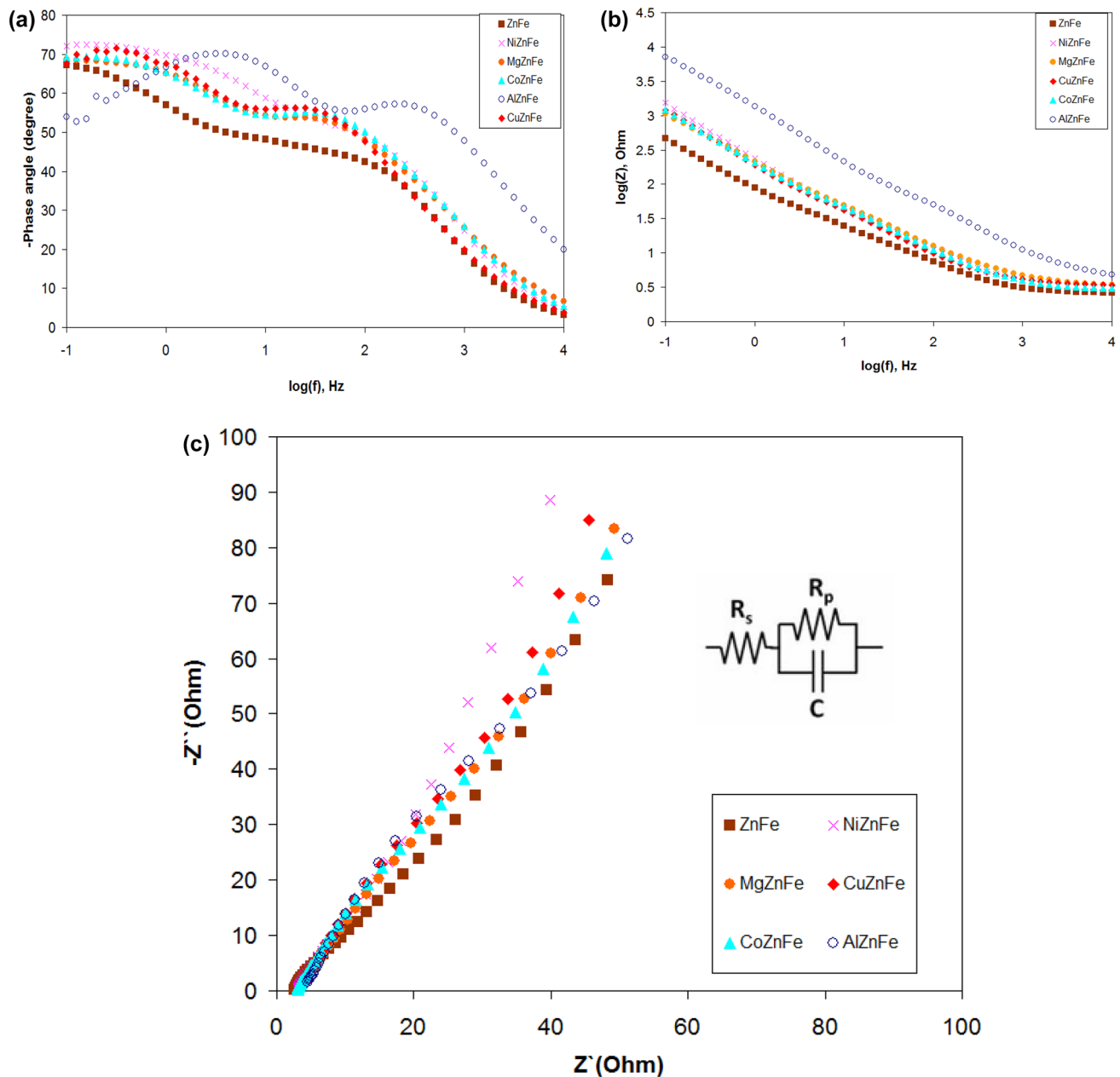
Fig. 13 Impedance spectroscopy plots of prepared electrodes at 150 °C for 5 h at 10,000 to 0.1 Hz sweep. The equivalent electrical circuit is shown and consisted of a resistor in series with a parallel combination of a resistor and capacitor

analyzed using Nyquist, Phase and Bode plots where each data point is obtained in a different frequency. As is shown in Fig. 13a, with decreasing the frequencies, all the electrodes phase angle approaches to − 90° indicating better capacitive behavior. Invariable impedance amplitude is recorded in Fig. 13 b in the high frequencies for all the electrodes indicating an equivalent solution resistance for them. The Nyquist data (Fig. 13c) are modeled by an equivalent circuit (inset in Fig. 13c), where, R_s is affected by the electrolyte and active materials resistivity as well as

the electrode and current collector interface quality [64, 65]. R_{ct} is the charge-transfer resistance of the electrodes during cycling. All the Nyquist plots consist of a quasi-semicircle in their high frequencies revealing the charges transfer phenomena at the electrode/electrolyte interface. A constant line at low frequencies assign to the diffusion of ions in the electrolyte [66]. The R_s and R_{ct} are calculated from the Nyquist plot (Fig. 13c) and are shown in Table 3. The R_{ct} value of the energy storages increases in order of ZnFe < NiZnFe < MgZnFe < CuZnFe < CoZnFe < AlZnFe.

Table 3 Electrochemical performance of MTTMF electrode

Parameter	ZnFe	NiZnFe	MgZnFe	CuZnFe	CoZnFe	AlZnFe
R_s (Ω)	2.9	3	3.4	3.4	3	3.1
R_{ct} (Ω)	2.9	3.4	3.6	3.8	3.8	4.1
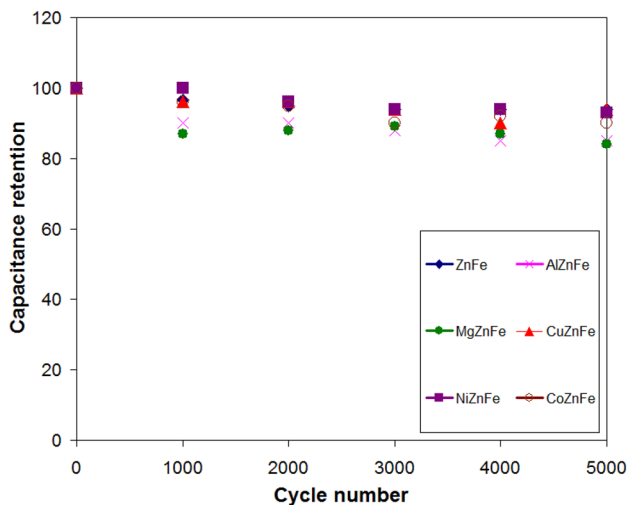
Fig. 14 Variation of the capacitance retention of electrodes as a function of cycle number

Cycling life is a main parameter that determines the practical applications of all the storage devices such as supercapacitors and batteries. Figure 14 shows variation of the capacitance retention of electrodes as a function of the cycle number. As shown in this figure, after 5000 continuous cycling, the specific capacitances were revealed to be 94%, 90%, 94%, 93%, 85% and 84% of their initial value for ZnFe, CoZnFe, CuZnFe, NiZnFe, AlZnFe and MgZnFe electrodes, respectively. Relatively good cycling stability of this electrode could be attributed to electrochemical stability of the active materials and proper contact between the current collector and the electrode materials because of direct growth of active nanostructures of the electrode on the substrate surface. The ZnFe electrode shows the best cycling stability and this sample shows the highest specific capacitance as compared to other electrodes.

4 Conclusion

Innovative MTTMF nanocomposites have been synthesized via a facile hydrothermal procedure combining a post-annealing treatment on nickel foam substrate. It has been concluded that temperature increasing resulted in positive effects on morphologies and electrochemical behavior of the MTTMF nanomaterials. Single-phase formation of spinel ferrites was characterized by the XRD analysis. SEM images revealed porous structures with high electrochemical active sites that enable electrolyte ions transfer. Among all the electrodes, ZnFe presented better pseudocapacitive behavior in 1 M KOH aqueous electrolyte.

Compliance with ethical standards

Conflict of interest The authors declare that they have no conflict of interest.

Ethical approval This article does not contain any studies with human participants or animals performed by any of the authors.

References

1. Brezesinski T, Wang J, Tolbert Sh, Dunn B (2010) Ordered mesoporous alpha-MoO_3 with iso-oriented nanocrystalline walls for thin-film pseudocapacitors. Energy Environ Sci J 9(2):146–151
2. Wu ZS, Sun Y, Tan YZ, Yang S, Feng X, Müllen JK (2012) Sustainable activated carbon fibers from liquefied wood with controllable porosity for high-performance supercapacitors. J Mater Chem A 134:19532–19535
3. Tarascon JM, Armand M (2001) Issues and challenges facing rechargeable lithium batteries. Nature 414:359–367
4. Pasquier AD, Plitz I, Gural J, Menocal S, Amatucci G (2003) Characteristics and performance of 500 F asymmetric hybrid advanced supercapacitor prototypes. J Power Sources 113:62–71
5. Yao X, Zhao C, Kong J, Wu H, Zhoua D, Lu X (2014) Dopamine-assisted one-pot synthesis of zinc ferrite-embedded porous carbon nanospheres for ultrafast and stable lithium ion batteries. J Chem Commun 50(93):14597–14600
6. Yang M-Q, Zhang Y, Zhang N, Tang Z-R, Xu Y-J (2013) Visible-light-driven oxidation of primary C–H bonds over CdS with dual co-catalysts graphene and TiO_2. Sci Rep 3:2595
7. Huang G, Du X, Zhang F, Yin D, Wang L (2015) A facile molten-salt route for large-scale synthesis of $NiFe_2O_4$ nanoplates with enhanced lithium storage capability. Chem A Eur J 21(40):14140–14145
8. Wang Y, Park J, Sun B, Ahn H, Wang G (2012) Wintersweet-flower-like $CoFe_2O_4$/MWCNTs hybrid material for high-capacity reversible lithium storage. Chem-Asian J 7(8):1940–1946
9. Nilmoung S, Sinprachim T, Kotutha I, Kidkhunthod P, Yimnirun R, Rujirawat S, Maensiri S (2016) Electrospun carbon/$CuFe_2O_4$

composite nanofibers with improved electrochemical energy storage performance. J Alloys Compd 688:1131–1140

10. Thankachan RM, Rahman MM, Sultana I, Glushenkov AM, Thomas S, Kalarikkal N, Chen Y (2015) Enhanced lithium storage in $ZnFe_2O_4$–C nanocomposite produced by a low-energy ball milling. J Power Sources 282:462–470

11. Zhou Q, Xing J, Gao Y, Lv X, He Y, Guo Z, Li Y (2014) Ordered assembly of $NiCo_2O_4$ multiple hierarchical structures for high-performance pseudocapacitors. ASC Mater Interfaces 6:11394–11402

12. Wang S, Pu J, Tong Y, Cheng Y, Gao Y, Wang Z (2014) $ZnCo_2O_4$ nanowire arrays grown on nickel foam for high-performance pseudocapacitors. J Mater Chem A 2(15):5434–5440

13. Kumbhar VS, Jagadale AD, Shinde NM, Lokhande CD (2012) Chemical synthesis of spinel cobalt ferrite ($CoFe_2O_4$) nanoflakes for supercapacitor application. Appl Surf Sci 259:39–43

14. Gunjakar JL, More AM, Gurav KV, Lokhande CD (2008) Chemical synthesis of spinel nickel ferrite ($NiFe_2O_4$) nano-sheets. Appl Surf Sci 254:5844–5848

15. Chen KHJ, Liu S (2009) Hydrothermal preparation of octadecahedron Fe_3O_4 thin film for use in an electrochemical supercapacitor. Elechtrochem Acta 55:1–55

16. Raut SS, Sankapal BR (2016) First report on synthesis of $ZnFe_2O_4$ thin film using successive ionic layer adsorption and reaction: approach towards solid-state symmetric supercapacitor device. Electrochim Acta 198:203–211

17. Ravinder DE, Reddy AR (1999) Electrical transport properties of zinc-substituted manganese ferrites. Mater Lett 38(4):265–269

18. Bhujun B, Tan MT, Shanmugam AS (2017) Results in physics study of mixed ternary transition metal ferrites as potential electrodes for supercapacitor applications. Results Phys 7:345–353. https://www.sciencedirect.com/science/article/pii/S2211379716300134

19. Mohamed SG, Chen CJ, Chen CK, Hu SF, Liu RS (2014) High-performance lithium-ion battery and symmetric supercapacitors based on $FeCo_2O_4$ nanoflakes electrodes. ACS Appl Mater Interfaces 6:22701–22708

20. Sharma Y, Sharma N, Rao GS, Chowdari BVR (2008) Li-storage and cyclability of urea combustion derived $ZnFe_2O_4$ as anode for Li-ion batteries. Electrochem Acta 53:2380–2385

21. Liu B, Liu B, Wang Q, Wang X, Xiang Q, Chen D, Shen G (2013) New energy storage option: toward $ZnCo_2O_4$ nanorods/nickel foam architectures for high-performance supercapacitors. ASC Appl Mater Interfaces 5:10011–10017

22. Bao F, Wang X, Zhao X, Wang Y, Ji Y, Zhang H, Liu X (2014) Controlled growth of mesoporous $ZnCo_2O_4$ nanosheet arrays on Ni foam as high-rate electrodes for supercapacitors. RSC Adv 4(4):2393–2397

23. Zhou G, Zhu J, Chen Y, Mei L, Duan X, Zhang G, Chen L, Wang T, Lu B (2014) Simple method for the preparation of highly porous $ZnCo_2O_4$ nanotubes with enhanced electrochemical property for supercapacitor. Electrochim Acta 123:450–455

24. Purushothaman KK, Manohara Babu I, Sethuraman B, Muralidharan G (2013) Nanosheet-assembled NiO microstructures for high-performance supercapacitors. ASC Appl Mater Interfaces 5:10767–10773

25. Chen H, Zhang Q, Wang J, Wang Q, Zhou X, Li X, Yang Y, Zhang K (2014) Mesoporous $ZnCo_2O_4$ microspheres composed of ultrathin nanosheets cross-linked with metallic NiSix nanowires on Ni foam as anodes for lithium ion batteries. Nano Energy 10:245–258

26. Li J, Wang J, Wexler D, Shi D, Liang J, Liu H, Xiong S, Qian Y (2013) Simple synthesis of yolk-shelled $ZnCo_2O_4$ microspheres towards enhancing the electrochemical performance of lithium-ion batteries in conjunction with a sodium carboxymethyl cellulose binder. J Mater Chem A 1(48):15292–15299

27. Cottineau T, Toupin M, Delahaye T, Brousse T, Bélanger D (2006) Nanostructured transition metal oxides for aqueous hybrid electrochemical supercapacitors. Appl Phys A 82(4):599–606

28. Gupta V, Gupta S, Miura N (2008) Potentiostatically deposited nanostructured CoxNi1 – x layered double hydroxides as electrode materials for redox-supercapacitors. J Power Sources 175(1):680–685

29. Zhu M, Zhang X, Zhou Y, Zhuo C, Huang J, Li S (2015) Facile solvothermal synthesis of porous $ZnFe_2O_4$ microspheres for capacitive pseudocapacitors. RSC Adv 5(49):39270–39277

30. Komarneni S, Fregeau E, Breval E, Roy R (1988) Hydrothermal preparation of ultrafine ferrites and their sintering. J Am Ceram Soc 71(1):C-26

31. Sankaranarayanan VK, Sreekumar C (2003) Precursor synthesis and microwave processing of nickel ferrite nanoparticles. Curr Appl Phys 3:205–208

32. D'Arrigo CLMC, Pellacani GC (1998) Microwave-hydrothermal synthesis of nanophase ferrites. J Am Ceram Soc 81(11):3041–3043

33. Kamnev AA, Ristić M (1997) Fourier transform far-infrared spectroscopic evidence for the formation of a nickel ferrite precursor in binary Ni(II)–Fe(III) hydroxides on coprecipitation. J Mol Struct 408:301–304

34. Thimmaiah S, Rajamathi M, Singh N, Bera P, Meldrum F, Chandrasekhar N, Seshadri R (2001) A solvothermal route to capped nanoparticles of γ-Fe_2O_3 and $CoFe_2O_4$. J Mater Chem 11(12):3215–3221

35. Kolekar CB et al (1995) Effect of Gd3 + substitution on dielectric behaviour of copper- cadmium ferrites. J Mater Sci 30(22):5784–5788

36. Chen D, Chen D, Jiao X, Zhao Y, He M (2003) Hydrothermal synthesis and characterization of octahedral nickel ferrite particles. Powder Technol 133:247–250

37. Albuquerque AS, Ardisson JD, Macedo WA, Lopez JL, Paniago R, Persiano AI (2001) Structure and magnetic properties of nanostructured Ni-ferrite. J Magn Magn Mater 226–230:1379–1381

38. Kale SGA, Misra RDK (2004) Magnetic behavior of nanocrystalline nickel ferrite synthesized by the reverse micelle technique. J Magn Magn Mater 277:350–358

39. Reddy KM, Satyanarayana L, Manorama SV, Misra RD (2004) A comparative study of the gas sensing behavior of nanostructured nickel ferrite synthesized by hydrothermal and reverse micelle techniques. Mater Res Bull 39:1491–1498

40. Lin Y, Wang J, Yang H, Wang L, Cao M (2017) Comparative study of individual aqueous electrolytes with porous $ZnFe_2O_4$ for supercapacitor. Mater Lett 207:195–197

41. Byrappa K, Yoshimura M (2001) Handbook of hydrothermal technology A technology for crystal growth and materials Pprocessing. https://www.sciencedirect.com/book/9780815514459/handbook-of-hydrothermal-technology#book-description

42. Konishi TNY, Mizoe K (2004) A new synthesis route from spent sulfuric acid pickling solution to ferrite nanoparticles. Hydrometallurgy 74:57–65

43. Yi X, Yitaia Q, Jinga L, Zuyaoa C, Li Y (1995) Hydrothermal preparation and characterization of ultrafine powders of ferrite spinels MFe_2O_4 (M = Fe, Zn and Ni). Mater Sci Eng, B 34:L1–L3

44. Salunkhe RR, Jang K, Lee SW, Ahn H (2012) Aligned nickel-cobalt hydroxide nanorod arrays for electrochemical pseudocapacitor applications. RSC Adv 2:3190–3193

45. Vam B (1969) Infrared spectra of cubic and tetragonal manganese ferrites. Phys Status Solidi (b) 33(2):563–572

46. Modi KB, Chhantbar MC, Joshi HH (2006) Study of elastic behaviour of magnesium ferri aluminates. Ceram Int 32(2):111–114

47. Rahman MM, Khan SB, Faisal M, Asiri AM, Alamry KA (2012) Highly sensitive formaldehyde chemical sensor based on hydrothermally prepared spinel $ZnFe_2O_4$ nanorods. Sens Actuators B: Chem 171:932–937

48. Nie G, Lu X, Chi M, Gao M, Wang C (2018) General synthesis of hierarchical C/MOx@MnO_2 (M = Mn, Cu, Co) composite nanofibers for high-performance supercapacitor electrodes. J Colloid Interface Sci 509:235–244

49. Al P (1939) The Scherrer formula for X-ray particle size determination. Phys Rev 56(10):978–982

50. Lee JW, Hall AS, Kim JD, Mallouk TE (2012) A facile and template-free hydrothermal synthesis of Mn_3O_4 nanorods on graphene sheets for supercapacitor electrodes with long cycle stability. Chem Mater 24(6):1158–1164

51. Sankapal BR, Gajare HB, Dubal DP, Gore RB, Salunkhe RR, Ahn H (2014) Presenting highest supercapacitance for TiO_2/MWNTs nanocomposites: novel method. Chem Eng J 247:103–110

52. Brousse T, Belanger D, Long JW (2015) To be or not to be pseudocapacitive? J Electrochem Soc 162(5):A5185–A5189

53. Lokhande CD, Dubal DP, Joo OS (2018) Metal oxide thin film based supercapacitors. Curr Appl Phys 11(3):255–270

54. Liu H, Guo Y, Zhang Y, Wu F, Liu Y, Zhang D (2013) Synthesis and properties of $ZnFe_2O_4$ replica with biological hierarchical structure. Mater Sci Eng, B 178(16):1057–1061

55. Lin Y, Zhang J, Li M, Wang L, Yang H (2017) An excellent strategy for synthesis of coral-like $ZnFe_2O_4$ particles for capacitive pseudocapacitors. J Alloy Compd 726:154–163

56. Raut SS, Sankpal BR (2016) first report on synthesis of $ZnFe_2O_4$ thin film using successive ionic layer adsorption and reaction. Electrochem Acta 198:203–211

57. Vadiyar MM, Kolekar SS, Chang J-Y, Kashale AA, Ghule AV (2016) Reflux condensation mediated deposition of Co_3O_4 nanosheets and $ZnFe_2O_4$ nanoflakes electrodes for flexible asymmetric supercapacitor. Electrochim Acta 222:1604–1615

58. Vadiyar MM, Kolekar SS, Deshpande NG, Chang J-Y, Kashale AA, Ghule AV (2017) Binder-free chemical synthesis of $ZnFe_2O_4$ thin films for asymmetric supercapacitor with improved performance. Ionics 23(3):741–749

59. Yang S, Han Z, Sun J, Yang X, Hu X, Li C, Cao B (2018) Controllable $ZnFe_2O_4$/reduced graphene oxide hybrid for high-performance supercapacitor electrode. Electrochim Acta 268:20–26

60. Agyemang FO, Kim H (2016) Electrospun $ZnFe_2O_4$-based nanofiber composites with enhanced supercapacitive properties. Mater Sci Eng, B 211:141–148

61. Sivakumar N et al (2011) Nanostructured $MgFe_2O_4$ as anode materials for lithium-ion batteries. J Alloy Compd 509(25):7038–7041

62. Sen P, De A (2010) Electrochemical performances of poly(3,4-ethylenedioxythiophene)–$NiFe_2O_4$ nanocomposite as electrode for supercapacitor. Elechtrochem Acta 55(16):4677–4684

63. Uchaikin VV, Sibatov RT, Ambrozevich AS (2016) On impedance spectroscopy of supercapacitors. Russ Phys J 59(6):845–855

64. Yuan YF et al (2011) Nickel foam-supported porous $Ni(OH)_2$/NiOOH composite film 620 as advanced pseudocapacitor material. Electrochim Acta 56(6):2627–2632

65. Huang MLN et al (2014) Nanoflakes grown on porous graphene frameworks as advanced electrochemical pseudocapacitor materials. J Power Sources 623(259):98–105

66. Li N, Shan D, Xue H (2007) Electrochemical synthesis and characterization of poly 617 (pyrrole-co-tetrahydrofuran) conducting copolymer. Eur Polym J 43(6):2532–2539